Determination of the 3D shape of a nanoscale crystal with atomic resolution from a single image

C. L. Jia[1,2,3]*†, S. B. Mi[1]†, J. Barthel[3,4], D. W. Wang[1], R. E. Dunin-Borkowski[2,3], K. W. Urban[2,3] and A. Thust[2,3]

Although the overall atomic structure of a nanoscale crystal is in principle accessible by modern transmission electron microscopy, the precise determination of its surface structure is an intricate problem. Here, we show that aberration-corrected transmission electron microscopy, combined with dedicated numerical evaluation procedures, allows the three-dimensional shape of a thin MgO crystal to be determined from only one single high-resolution image. The sensitivity of the reconstruction procedure is not only sufficient to reveal the surface morphology of the crystal with atomic resolution, but also to detect the presence of adsorbed impurity atoms. The single-image approach that we introduce offers important advantages for three-dimensional studies of radiation-sensitive crystals.

The accurate description of the physical and chemical properties of nanoscale materials is a long-standing goal in nanoscience and technology. Many of the interesting properties of such dimensionally limited systems result from the dominant part played by their surface structure and chemistry, which are related intimately to their functionality[1]. An important example is the use of nanoparticles in catalysis, where the chemical reactivity depends on both the atomic species and the particular atom arrangement present on the surface[2–4].

Aberration-corrected transmission electron microscopy is a powerful tool for studying the bulk structure of crystalline materials, as the recorded images provide sensitive information about the lateral positions of the atomic columns imaged end-on[5]. This holds for both instrumental modes of transmission electron microscopy, the coherent imaging mode (TEM) and the scanning mode (STEM). However, the information that has been provided by these techniques about the structure of surfaces has remained limited[6]. This is due to the fact that TEM is usually not very sensitive to the particular atomic arrangement on the top and bottom surfaces of a specimen. In TEM, the number of atoms in individual atomic columns[7–9] and the fraction of impurity atoms or vacancies have been measured by applying the exit-plane wavefunction reconstruction technique to a focal series of images[10,11]. In STEM, atom-counting techniques make use of a quantitative comparison between experimental and calculated image intensity distributions[12,13]. Recently, the successful three-dimensional location of single dopant atoms has been reported using the STEM technique[14,15]. Electron holography has also been used to measure the local thickness of a sample with single-atom precision[16]. However, none of these techniques have yet allowed unambiguous conclusions to be drawn about both the thickness and the surface structure of a sample, let alone for the top and bottom surfaces to be distinguished in the viewing direction. A feasible route is provided by electron tomography on the basis of a number of images taken along different viewing

directions. By employing the discrete tomography technique in STEM, the three-dimensional shape of a Ag particle embedded in an Al matrix could be determined[17]. This technique assumes prior knowledge of the particle's atomic lattice structure, and successful reconstruction required at least two images. More recently, STEM tomography has been applied to reconstruct the structure of a Au and a Pt particle on the basis of 69 and 104 individual projections, respectively[18,19]. Although atomic-resolution information was obtained about the bulk material, even including crystal defects, the resolution remained limited with respect to the surface structure, and tomography experiments remain very demanding when true atomic resolution is the goal[20–22]. The need to acquire a large number of images under high-resolution conditions and to align them in a consistent way is challenging, particularly in view of the inaccuracy of tilting specimen holders and the limited optical stability of the microscope operating in the ångström regime[23,24]. Furthermore, the high electron dose required by electron tomography may damage the atomic structure of interest, making a consistent reconstruction of the object impossible.

Here we report on the experimental three-dimensional (3D) shape reconstruction of a thin MgO crystal with single-atom precision from only a single image. Our approach follows a different route from the classical tomographic multi-image approach. At the same time, we demonstrate that single-atom sensitivity is obtainable not only for high nuclear charge elements, as studied in previous works[7–9,12–19], but can be extended to include light chemical elements, such as oxygen. The latter aspect is of considerable practical relevance because oxygen plays a key role as an anionic constituent in many technologically relevant materials[25]. We restrict our treatment to the case of a periodic crystal which does not contain impurities or vacancies in significant density[26,27]. These assumptions are identical to those made in earlier studies[12,13,16–19].

Three-dimensional reconstruction from a single high-resolution TEM image is possible owing to the fact that the physical principle of electron diffraction is an intrinsically 3D process[28]. We demonstrate

[1]International Center for Dielectric Research, Xi'an Jiaotong University, Xi'an 710049, China, [2]Peter Grünberg Institute, Forschungszentrum Jülich GmbH, 52425 Jülich, Germany, [3]Ernst Ruska-Centre for Microscopy and Spectroscopy with Electrons, Forschungszentrum Jülich GmbH, 52425 Jülich, Germany, [4]Central Facility for Electron Microscopy, RWTH Aachen University, Ahornstr. 55, 52074 Aachen, Germany. †These authors contributed equally to this work. *e-mail: c.jia@fz-juelich.de

that the signal that is related to the 3D nature of electron diffraction can be recorded and interpreted by combining three major methodical building blocks. The first building block is the choice of a highly sensitive imaging mode for experimental data acquisition. The second building block is a structure refinement procedure, in which a structure model and the optical parameters are varied stepwise in such a way that the image calculated on this basis provides a best fit to the experimental image. A very important feature of this refinement procedure is the use of absolute image intensity levels[29,30] instead of commonly used relative values (see Supplementary Information for details). The third building block is a statistical confidence check that provides precise quantitative statements about the uniqueness of the final 3D structure model.

The image of MgO shown in Fig. 1a was acquired along the [001] crystal direction using the negative spherical aberration imaging (NCSI) technique. This technique provides high contrast that is localized, to the greatest possible extent, at the positions of the atomic columns (seen end-on), which appear as bright on a dark background[31,32]. Figure 1b shows a magnification of the upper region of Fig. 1a. The false-colour display emphasizes the intensity variations, while the dashed lines separate regions of significantly different peak intensity, which can be interpreted as evidence for surface steps. The peak intensity values contain information not only about the composition (number of Mg and O atoms) in each atomic column, but also about its relative position along the crystallographic z-direction and about the type of atom that occupies the upper and lower surface sites. Access to this information is obtained in a data refinement procedure. In this procedure, we take into account the fact that the peak intensity values measured in Fig. 1a are in general not linearly related to the number of alternating Mg and O atoms within a given atomic column. Moreover, the peak positions do not coincide exactly with the real column positions. Possible reasons for such deviations include unavoidable misalignment of the crystallographic axis with respect to the incident electron beam direction[33] and unavoidable residual optical lens aberrations present during image acquisition[23,24].

To exploit even very weak contrast details and to enable quantitative determination of the atomic structure underlying the image, an iterative fitting procedure is employed. This iterative fitting procedure is applied to the region surrounded by the dashed line in Fig. 1a and is executed in two steps. In the first step, an ideally flat MgO crystal is assumed. All globally effective parameters are refined, such as the mean specimen thickness, the specimen misorientation, the effective absorption constant (Supplementary Fig. 1) and optical aberrations of the microscope[30]. Instrumental properties that can be measured independently, such as the frequency modulation transfer function of the microscope's charge-coupled device (CCD) camera and the defocus spread of the microscope defining the achievable resolution[29,34], are also incorporated into the simulation at this stage.

In the second step of the fitting procedure, the local properties of the sample are further refined. This refinement includes not only the x- and y-coordinates and the occupancies of the individual atomic columns, but in particular also their z-positions. At the same time, the globally effective parameters that were estimated in the first step are also further refined. The final global parameters are compiled in Supplementary Table 1.

The fitting procedure relies on the simulated and experimental images being compared on the basis of absolute image intensities[29,30], where the root mean square (r.m.s.) difference of the intensity distributions is minimized as the figure-of-merit. Whereas globally effective parameters are refined using image comparisons over large areas, the unknown structure parameters of individual atom columns are determined from small image areas with dimensions
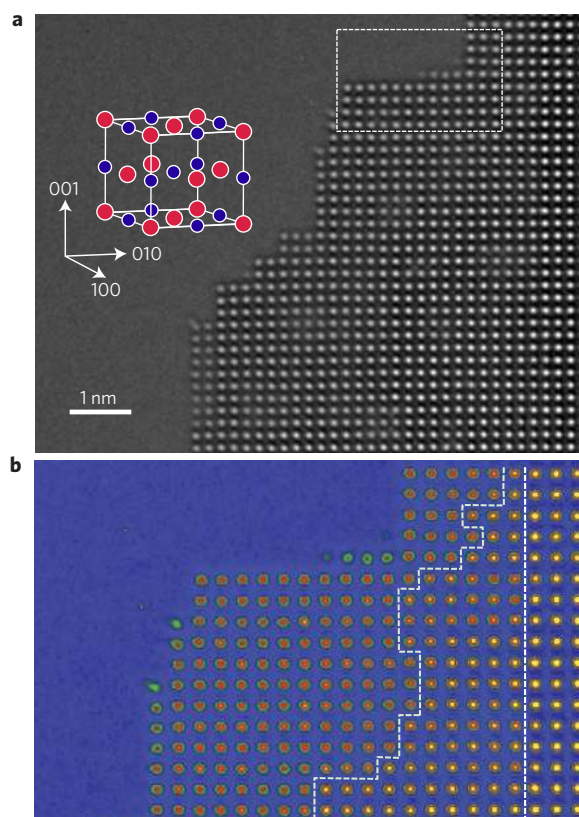
Figure 1 | Aberration-corrected high-resolution TEM image of an MgO crystal. a, Original image taken along the [001] crystallographic direction under negative spherical aberration imaging conditions. Projected atomic columns appear as bright dots on a dark background. Side terraces are visible at the boundary between vacuum (left) and the crystal (right). A perspective view of the MgO unit cell is shown in the inset.
b, Magnification of the upper part of **a**, with the recorded image intensity shown in false colour. Dashed lines separate regions of significantly different column intensity, indicating the presence of surface steps.

equal to or below the interatomic distance. An example of a combined refinement of local and global properties is demonstrated by Supplementary Fig. 2, where the occupation inversion problem is addressed. It is shown there that the local decision problem, whether the z-axis sequence of a certain local atom column is Mg–O–Mg–O …, or alternatively O–Mg–O–Mg …, can be solved unambiguously by the prior global evaluation of all columns containing an odd atom number.

Figure 2a shows the selected region of the experimental image in Fig. 1a. For comparison, the best-fitting image simulated on the basis of the refined structure model is shown in Fig. 2b. A quantitative illustration of the quality of the match achieved between the experimental and simulated peak intensity values is given in Fig. 2c. The residual differences δ_{int} between the experimental and simulated peak intensities are shown in Fig. 2d. Inspection of Fig. 2d indicates that the addition or removal of a single Mg or O atom from an atomic column can be detected, as this action causes an average change in the absolute peak intensity value of 0.052, which is much larger than the residual fit discrepancy $\sigma_f = 0.0053$ (r.m.s.) and is also larger than the vacuum noise variation $\sigma_n = 0.013$ (r.m.s.). It is important that the signal resulting from the addition or removal of a single atom is four times higher than the experimental noise level, as this means that the detection sensitivity can be extended formally even towards half-occupied lattice sites. For this reason, the possibility of a formal occupancy of 50% at the surface sites is
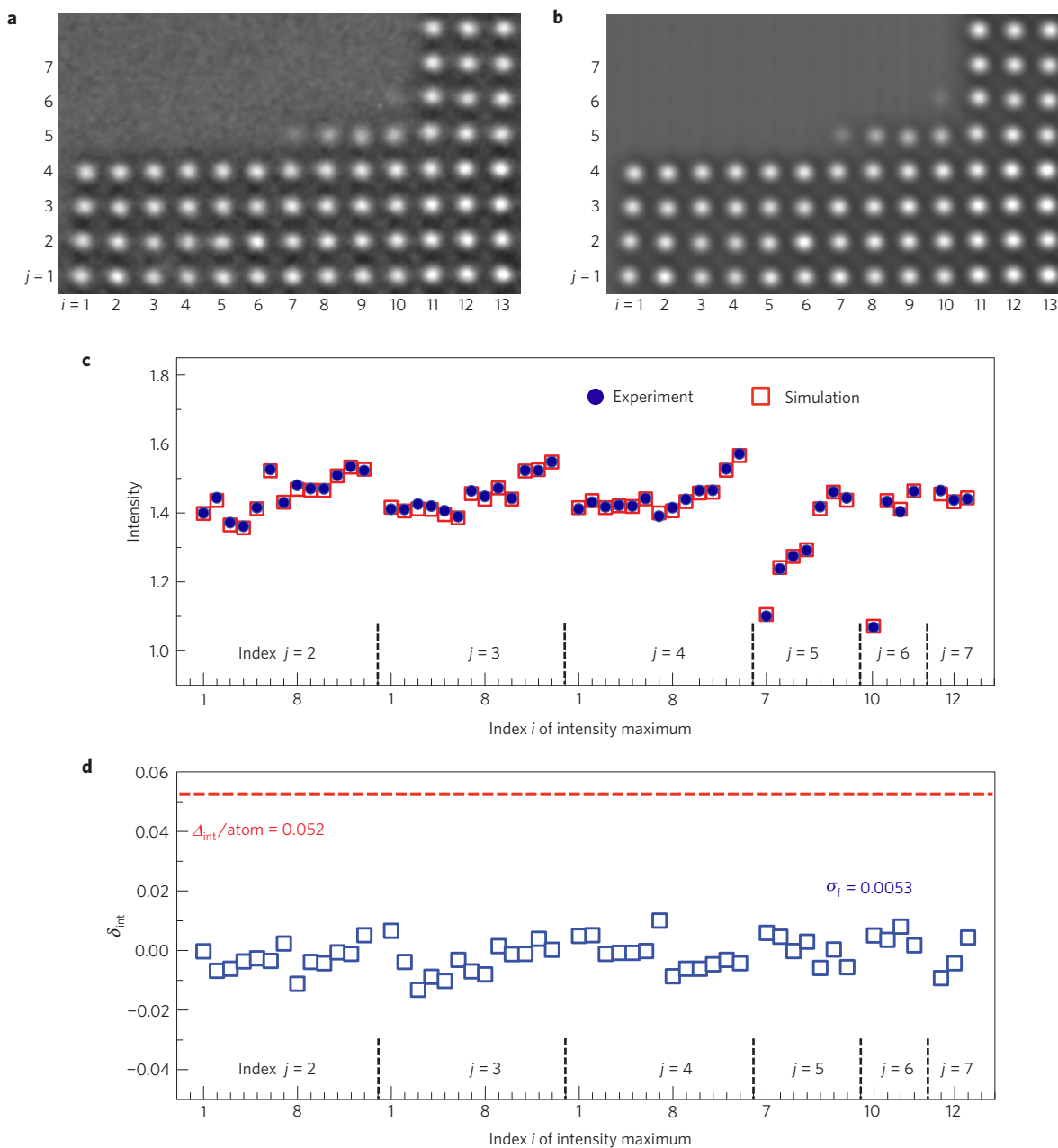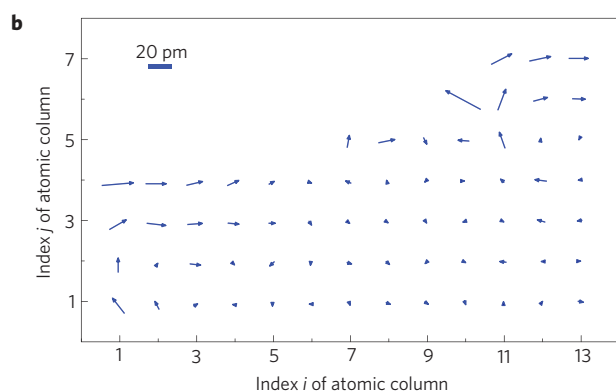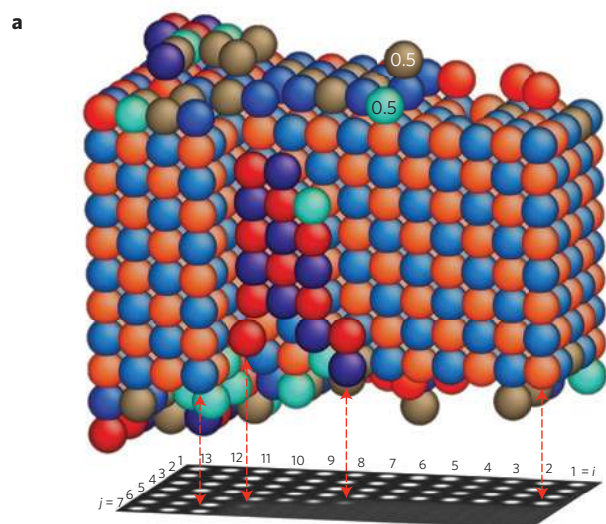
Figure 2 | Comparison of experiment with simulation. a, Experimental image taken from the framed region in Fig. 1a. **b**, Best-fitting simulated image shown on the same intensity scale. The individual intensity maxima are indexed according to their positions (i,j). **c**, Quantitative comparison of experimental (full circles) and simulated (open squares) peak intensities, normalized with respect to the mean intensity of the image. The peak intensities are extracted from small areas of 100 image pixels by fitting a Gaussian peak function to local intensity distributions around the maxima. **d**, Residual difference δ_{int} between the fitted experimental and simulated peak intensities. The r.m.s. value of δ_{int} is $\sigma_f = 0.0053$. The dashed red line denotes the average increase of the peak intensity on adding a single atom ($\Delta_{int}/\text{atom} = 0.052$).

permitted in our refinement procedure. A line scan demonstrating the resulting fit between the experimental and simulated intensity distribution is shown in Supplementary Fig. 3. The refinement of the (x,y) positions of the atomic columns was performed to an accuracy of better than 1 pm (Supplementary Fig. 4), and z-position changes by ± 1 atomic plane could be detected in the presence of image noise (Supplementary Fig. 5).

Figure 3a shows the refined atomic model as a main outcome of the 3D shape reconstruction. The decisive progress made here is that the morphology of the top and bottom surfaces can now be resolved separately and shown with atomic precision, including even the light oxygen atoms. The surface atoms that are shown in

brown and cyan denote formally half-occupied Mg and O sites, respectively. Furthermore, atom column displacements away from the ideal lattice positions in the (x,y)-plane are resolved and shown in the form of a vector diagram in Fig. 3b, where the ideal lattice is determined by assuming perfect periodicity and by averaging the unit cells in an image area away from the sample edge. Systematic atomic column displacements of the order of 20 pm or larger can be seen to occur at the sample edge.
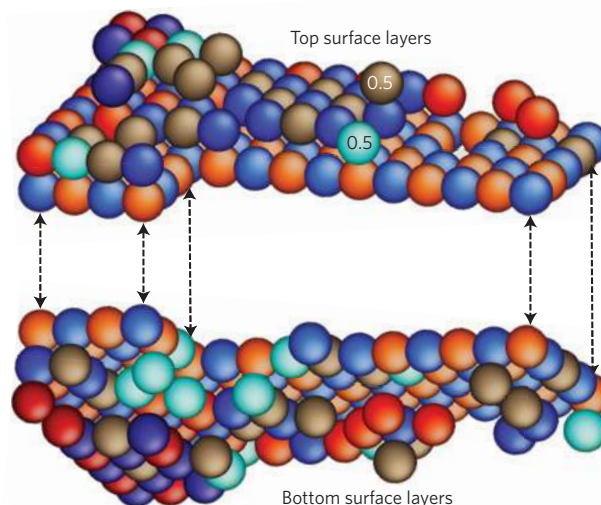
It is of crucial importance to assess the correctness of the final 3D structure model quantitatively. Such an assessment step forms the third building block of our reconstruction procedure. The strategy of simply taking the best-fitting simulation as an indicator

Figure 4 | Perspective view of the top and bottom surface layers reproduced from the 3D structure of Fig. 3a. Both the top and the bottom surfaces consist of 82 lattice sites in the shown region. The top surface contains 20 half-occupied sites, with an Mg:O site ratio of 16:4. The bottom surface contains 26 half-occupied sites, with an Mg:O site ratio of 15:11. On both surfaces, the formally half-occupied Mg sites are thus in a clear majority.

Figure 3 | Determined 3D atomic arrangement and displacements of atoms. a, Atomically resolved view of the best-fitting 3D atomic arrangement for the sample region shown in Fig. 2a. Red spheres indicate fully occupied Mg sites and blue spheres fully occupied O sites. Increased colour saturation is used to highlight surface atoms. In the surface layers, brown spheres indicate formally half-occupied Mg sites, while cyan spheres indicate formally half-occupied O sites. **b**, Vector map showing the displacements of the best-fitting atomic column positions in the image plane away from their ideal periodic positions. The arrowheads point in the directions of the displacements. The lengths of the arrows indicate the magnitudes of the displacements.

of the correct solution could potentially fail owing to uniqueness problems, whereby two different column configurations could produce the same or nearly the same image contrast, which could no longer be identified uniquely in the presence of noise. To exclude such potential sources of error, we developed a statistical analysis procedure based on the Monte Carlo principle (Supplementary Information). A quantitative reliability measure for the chosen best-fit strategy can be obtained by simulating thousands of column recognition attempts in the presence of noise, and bookkeeping the number of correct and incorrect recognitions.

The main result of this Monte Carlo check is that nearly all possible atomic column configurations can indeed be identified reliably. With regard to atom content, the addition or removal of an atom to or from a column can always be detected. With respect to the column z-position, nearly all possible column configurations can be located with high confidence along the electron beam direction, as shown in Supplementary Fig. 9. In addition to the unique determination of the number of atoms n in one column, the

correct location of a column along the z-direction is possible with a confidence of 70% or better in most cases. Only in the cases $n = 1$ and $n = 2$, where a column consists of one or two atoms, does the achievable confidence decrease to 40%.

A possible explanation for finding formally half-occupied lattice sites at the crystal surfaces can be proposed by considering two different scenarios. In the first scenario, we assume that Mg and O atoms are mobilized by electron irradiation and occupy surface sites during only approximately 50% of the 0.5 s exposure time. In the second scenario, we assume that weakly scattering C atoms, instead of regular lattice Mg atoms, reside at the partially occupied surface sites. Both the dynamic surface migration scenario and the static carbon adsorption scenario result in similar improvements to the fit between simulations and experiment (Supplementary Fig. 10).

Further insight into the mechanism that may be responsible for the partial occupancies can be gained on the basis of two findings. First, formally half-occupied Mg sites occur more often than formally half-occupied O sites (Fig. 4). In the dynamic surface migration scenario, the observed asymmetry would require considerably higher surface mobility of Mg than O atoms, which we regard as unlikely. In the static carbon adsorption scenario, the observed asymmetry would require carbon to be adsorbed preferentially near Mg sites above occupied O sites. We therefore performed *ab initio* calculations to explore the possible site preference for the adsorption of C atoms (Supplementary Fig. 11). The results indicate a strong preference for the adsorption of C atoms directly above oxygen sites (Supplementary Table 2). It is known that carbon contamination cannot be avoided on the surfaces of MgO crystals even under high-vacuum conditions (pressure $> 10^{-7}$ Pa; ref. 35). Our findings are consistent with the fact that a structure model consisting of only fully occupied Mg and O sites is not expected.

In this work, we have successfully revealed the 3D shape of a nanoscale crystal from only one single experimental high-resolution TEM image. We have demonstrated that the surfaces of the crystal, in particular its top and bottom surfaces, can be analysed separately with single-atom precision, including weakly scattering

chemical species such as oxygen. The sensitivity achieved is high enough to detect the presence of impurity atoms adsorbed on the crystal surfaces.

The structural information about the z-axis distribution of atoms translates into very faint contrast details, which we exploit here up to the limits given by presently available instrumentation and by the thereby achievable signal-to-noise ratio. Because the signal-to-noise ratio depends on multiple factors, including camera sensitivity, accelerating voltage, electron dose resistance, mechanical stability and incoherent imaging envelopes, a sufficiently large 'signal distance' should exist between neighbouring solutions to obtain uniqueness in the structure retrieval. In the present case, a sufficiently large 'signal distance' is obtained by choosing a discrete atom lattice, which does not allow continuous intermediate z-positions. Similarly, the choice of two chemical elements which have a sufficiently large difference in their atomic charge numbers Z ($Z = 8$ for O and $Z = 12$ for Mg), and the exclusion of voids and impurity atoms, allow a sufficiently well separated signal output to be obtained for the possible structural configurations. It is very likely that the structural sensitivity of the method can be enhanced significantly by an increase of the achievable signal-to-noise ratio provided by improved instrumentation (for example, low-voltage microscopy, use of cooling or of ultrahigh vacuum). We emphasize that the present difference in atomic charge number $\Delta Z = 4$ is already small and that our assumption of the lack of voids and impurities is justified for commercial MgO (Methods).

Our single-image approach can be highly advantageous, or may indeed be the only alternative, when dealing with radiation-sensitive crystals, for which it is often impossible to acquire more than a single image before the atomic structure has changed. The possibility to detect changes in surface morphology during *in situ* chemical reactions is also now within reach owing to the advantage of using a very short acquisition time. The present single-image approach therefore offers broad application potential for atomically resolved 3D studies of nanoscale materials.

Methods

Specimen preparation and image acquisition. The specimen used for the present investigation is a single crystal of MgO. Typical impurity concentrations of approximately 100 at. ppm and typical vacancy concentrations of below 10^{14} cm^{-3} are reported in the literature for commercial MgO (refs 26,27). These values correspond to a relative impurity concentration of 10^{-4} and to a relative vacancy concentration of approximately 10^{-9}. The assumption of the absence of a significant amount of vacancies and impurities in the region of interest, made in the main text, is therefore considered to be well justified.

A TEM specimen was prepared by cutting a disc 3 mm in diameter from a single-crystalline MgO (001) wafer. This disc was then mechanically ground and dimpled close to its centre to a thickness of approximately 10 μm. To obtain a high-quality TEM specimen, further thinning of the sample was performed by Ar ion milling in a sample stage cooled by liquid nitrogen. During the final thinning process, the ion beam was set to a low energy to remove any ion-milling-induced amorphous surface layers as completely as possible.

An FEI Titan 80–300 microscope equipped with a corrector for the spherical aberration of the objective lens was used for HRTEM imaging at an accelerating voltage of 300 kV. Images were acquired using the NCSI technique, which yields strong image contrast that is localized as much as possible on the respective atomic columns[31,32]. Residual lens aberrations of the microscope were measured by the Zemlin tableau method and minimized shortly before image acquisition[23,36]. According to these measurements, the lens aberrations had the following coefficient values several minutes before HRTEM image acquisition: spherical aberration $C_S = -15$ μm, two-fold astigmatism $A_1 < 2$ nm, three-fold astigmatism $A_2 < 40$ nm and axial coma $B_2 < 30$ nm. The images were recorded in a defocus range between approximately $C_1 = +3$ nm and $C_1 = +6$ nm. A 2k × 2k GATAN UltraScan 1000 CCD camera was used for image acquisition.

Data processing and image simulation. Identification of intensity peak positions in the acquired HRTEM image, extraction of small image patches containing single intensity peaks and extraction of intensity line scans was performed using the iMtools software[37]. Simulation of high-resolution TEM images was carried

out using the MacTempas software[38]. High-resolution TEM images used for confidence evaluations were calculated using the Dr. Probe software[39]. Numerical procedures for adding realistic noise to the simulated images and Monte Carlo procedures were coded for the purpose of this work in the programming language Fortran 95.

References

1. Gleiter, H. Nanostructured materials: Basic concepts and microstructure. *Acta Mater.* **48**, 1–29 (2000).
2. Honkala, K. *et al.* Ammonia synthesis from first-principles calculations. *Science* **307**, 555–558 (2005).
3. Greenley, J. P. Active site of an industrial catalyst. *Science* **336**, 810–811 (2012).
4. Behrens, M. *et al.* The active site of methanol synthesis over Cu/ZnO/Al$_2$O$_3$ industrial catalysts. *Science* **336**, 893–897 (2012).
5. Urban, K. Studying atomic structures by aberration-corrected transmission electron microscopy. *Science* **321**, 506–510 (2008).
6. Erdman, N. *et al.* The structure and chemistry of the TiO$_2$-rich surface of SrTiO$_3$ (001). *Nature* **419**, 55–58 (2002).
7. Jinschek, J. R., Kisielowski, C., Van Dyck, D. & Geuens, P. *Measurement of The Indium Segregation in InGaN Based LEDs with Single Atom Sensitivity* Vol. 5187, 54–64 (Proc. SPIE, 2003).
8. Wang, A., Chen, F. R., Van Aert, S. & Van Dyck, D. Direct structure inversion from exit waves. Part I: Theory and simulation. *Ultramicroscopy* **110**, 527–534 (2010).
9. Wang, A., Chen, F. R., Van Aert, S. & Van Dyck, D. Direct structure inversion from exit waves. Part II: A practical example. *Ultramicroscopy* **116**, 77–85 (2012).
10. Jia, C. L., Thust, A. & Urban, K. Atomic-scale analysis of the oxygen configuration at a SrTiO$_3$ dislocation core. *Phys. Rev. Lett.* **95**, 225506 (2005).
11. Houben, L., Thust, A. & Urban, K. Atomic-precision determination of the reconstruction of a 90° tilt boundary in YBa$_2$Cu$_3$O$_{7-\delta}$ by aberration corrected HRTEM. *Ultramicroscopy* **106**, 200–214 (2006).
12. LeBeau, J. M., Findlay, S. D., Allen, L. J. & Stemmer, S. Standardless atom counting in scanning transmission electron microscopy. *Nano Lett.* **10**, 4405–4408 (2010).
13. Van Aert, S. *et al.* Procedure to count atoms with trustworthy single-atom sensitivity. *Phys. Rev. B* **87**, 064107 (2013).
14. Hwang, J. *et al.* Three-dimensional imaging of individual dopant atoms in SrTiO$_3$. *Phys. Rev. Lett.* **111**, 266101 (2013).
15. Ishikawa, R. *et al.* Three-dimensional location of a single dopant with atomic precision by aberration-corrected scanning transmission electron microscopy. *Nano Lett.* **14**, 1903–1908 (2014).
16. Linck, M., Freitag, B., Kujawa, S., Lehmann, M. & Niermann, T. State of the art in atomic resolution off-axis electron holography. *Ultramicroscopy* **116**, 13–23 (2012).
17. Van Aert, S. *et al.* Three-dimensional atomic imaging of crystalline nanoparticles. *Nature* **470**, 374–377 (2011).
18. Scott, M. C. *et al.* Electron tomography at 2.4-ångström resolution. *Nature* **483**, 444–447 (2012).
19. Chen, C-C. *et al.* Three-dimensional imaging of dislocations in a nanoparticle at atomic resolution. *Nature* **496**, 74–77 (2013).
20. Wang, A., Van Aert, S., Goos, P. & Van Dyck, D. Precision of three-dimensional atomic scale measurements from HRTEM images: What are the limits? *Ultramicroscopy* **114**, 20–30 (2012).
21. Bals, S., Van Aert, S. & Van Tendeloo, G. High resolution electron tomography. *Curr. Opin. Solid State Mater. Sci.* **17**, 107–114 (2013).
22. Bar Sadan, M. *et al.* Toward atomic-scale bright-field electron tomography for the study of fullerene-like nanostructures. *Nano Lett.* **8**, 891–896 (2008).
23. Barthel, J. & Thust, A. Aberration measurement in HRTEM: Implementation and diagnostic use of numerical procedures for the highly precise recognition of diffractogram patterns. *Ultramicroscopy* **111**, 27–46 (2010).
24. Barthel, J. & Thust, A. On the optical stability of high-resolution transmission electron microscopes. *Ultramicroscopy* **134**, 6–17 (2013).
25. US National Research Council *Condensed Matter and Materials Physics* (National Academy Press, 1999).
26. Klein, M. J. & Gager, W. B. Generation of vacancies in MgO by deformation. *J. Appl. Phys.* **37**, 4112–4116 (1966).
27. Mizuno, M., Araki, H., Shirai, Y., Oba, F. & Tanaka, I. Identification of Mg vacancy in MgO by positron lifetime measurements and first-principles calculations. *Defect Diffusion Forum* **242–244**, 1–8 (2005).
28. Spence, J. C. H. *High-Resolution Electron Microscopy* 3rd edn (Oxford Univ. Press, 2007).

29. Thust, A. High-resolution transmission electron microscopy on an absolute contrast scale. *Phys. Rev. Lett.* **102,** 220801 (2009).
30. Jia, C. L. *et al.* Atomic-scale measurement of structure and chemistry of a single-unit-cell layer of LaAlO₃ embedded in SrTiO₃. *Microsc. Microanal.* **19,** 310–318 (2013).
31. Jia, C. L., Lentzen, M. & Urban, K. Atomic-resolution imaging of oxygen in perovskite ceramics. *Science* **299,** 870–873 (2003).
32. Jia, C. L., Houben, L., Thust, A. & Barthel, J. On the benefit of the negative-spherical-aberration imaging technique for quantitative HRTEM. *Ultramicroscopy* **110,** 500–505 (2010).
33. Urban, K. Is science prepared for atomic-resolution electron microscopy? *Nature Mater.* **8,** 260–262 (2009).
34. Barthel, J. & Thust, A. Quantification of the information limit of transmission electron microscopes. *Phys. Rev. Lett.* **101,** 200801 (2008).
35. Tsong, I. S. T. *et al.* Carbon on surfaces of magnesium and olivine single crystals Diffusion from the bulk or surface oxide contamination? *Phys. Chem. Miner.* **12,** 261–270 (1985).
36. Zemlin, F., Weiss, K., Schiske, P., Kunath, W. & Herrmann, K-H. Coma-free alignment of high resolution electron microscopes with the aid of optical diffractograms. *Ultramicroscopy* **3,** 49–60 (1978).
37. Houben, L. *iMtools Electron Microscope Image Processing Software* (Forschungszentrum Jülich, 2014); www.er-c.org/methods/software.htm
38. O'Keefe, M. A. & Kilaas, R. Advances in high-resolution image simulation. *Scanning Microsc. Suppl.* **2,** 225–244 (1988).
39. Barthel, J. *Dr. Probe—High-Resolution (S)TEM Image Simulation Software* (Forschungszentrum Jülich, 2014); www.er-c.org/barthel/drprobe/

Author contributions

S.B.M. prepared the specimen and performed the experimental investigation. C.L.J. interpreted the experimental results using comparisons with image simulations and determined the 3D atomic structure of the specimen. J.B. and A.T. performed image simulations and the statistical confidence analysis. D.W.W. performed *ab initio* calculations. A.T., C.L.J., J.B. and K.W.U. wrote the manuscript. C.L.J. and R.E.D-B. supervised the research. All the authors discussed the results and commented on the manuscript.

Additional information

Supplementary information is available in the online version of the paper. Reprints and permissions information is available online at www.nature.com/reprints. Correspondence and requests for materials should be addressed to C.L.J.

Competing financial interests

The authors declare no competing financial interests.